GPS Solutions (2020) 24:59
https://doi.org/10.1007/s10291-020-0973-5

ORIGINAL ARTICLE

Sky visibility estimation based on GNSS satellite visibility: an approach of GNSS-based context awareness

Haosheng Xu[1] · Li-Ta Hsu[1] · Debiao Lu[2] · Baigen Cai[2]

Received: 28 November 2019 / Accepted: 5 March 2020

Abstract
Global navigation satellite system (GNSS) positioning in urban areas does not currently provide accurate and stable performance because surrounding buildings can block and reflect satellite signals. However, if we can determine the environment in which the receiver is located, appropriate positioning can be applied. For example, GNSS real-time kinematic and 3D-mapping-aided GNSS (3DMA GNSS) are used for positioning in open sky and urban areas, respectively. Thus, the context awareness of the GNSS receiver is important. In fact, an urban canyon can be further categorized into different levels based on sky visibility. We propose an innovative algorithm based on this categorization, which can provide information on surrounding buildings and give an estimation of sky visibility from raw GNSS measurements. This idea was inspired by the use of low-orbit satellite data for remote sensing applications. The recent development of multi-GNSS has led to a notable increase in the number of navigation satellites. Crucially, the visibility of satellites and the blockage of line-of-sight satellite signals are representative of the surrounding environment. The visibility of satellites can be classified by machine learning techniques, and an accurate classification can afford an estimation that is close to the real-sky visibility, as derived from a 3D building model and ground truth location. To assess the sensitivity of our proposed sky visibility estimation algorithm, we simulate different classification accuracies to investigate their effect on the performance of the algorithm.

Keywords Context awareness · 3DMA GNSS · Urban canyons

Introduction

Positioning services based on global navigation satellite systems (GNSSs) are in worldwide daily use. An important application of such GNSS positioning is pedestrian navigation in cities. However, GNSS positioning performance in an urban canyon is not satisfactory, due to the surrounding buildings blocking or interfering with some satellite signals. This can lead to GNSS positioning errors of more than one hundred meters in urban areas (Hsu 2018).

3D-mapping-aided (3DMA) GNSS positioning is a popular approach for improving this urban GNSS positioning performance, in which 3D building models are used to predict the visibility of the satellite and simulate the transmitting path and carrier-to-noise ratio (C/N_0) of satellite signals. Then, satellites can be categorized as line-of-sight (LOS) or non-line-of-sight (NLOS), and the user position can be determined by a process called shadow matching, i.e., comparing the measured and predicted satellite visibility over hypothesized candidate locations (Groves 2011). The 3D building model of 3DMA GNSS is also used to predict the path delay and C/N_0 of NLOS reception and thus create a virtual pseudorange by ray tracing (Suzuki and Kubo 2012; Nicolás et al. 2013; Hsu et al. 2016). Moreover, the user position can be calculated by a process called likelihood-based 3DMA GNSS ranging, which involves determining the likelihood score from a comparison of the estimated pseudorange and measured pseudorange over many candidate locations (Groves and Adjrad 2017). Furthermore, likelihood-based 3DMA GNSS ranging can be integrated with shadow matching, to take advantage of the good across-street performance of shadow matching (Adjrad and Groves 2018).

✉ Li-Ta Hsu
lt.hsu@polyu.edu.hk

[1] Interdisciplinary Division of Aeronautical and Aviation Engineering, The Hong Kong Polytechnic University, Kowloon, Hong Kong

[2] School of Electronic and Information Engineering, Beijing Jiaotong University, Beijing, China

Published online: 16 March 2020

Recent research has shown that the performance of the above 3DMA GNSS positioning algorithm is highly dependent on sky visibility (Adjrad et al. 2018). Sky visibility is an index used to describe the percentage of the sky that is visible from a sky-pointing fish-eye camera and can be considered as representing the different levels of urban canyons. Thus, a fish-eye image is taken to represent sky visibility and is denoted a skymask. In the absence of fish-eye imagery, a skymask can also be formed from a skyplot based on a surrounding 3D building. Illustrations of a fish-eye camera image, a skymask from the fish-eye camera, and a skymask from the 3D building model are shown in Fig. 1.

Sky visibility for the skymask generated from the 3D building model is calculated by the elevation angle of the building boundary over each azimuth angle, expressed as

$$\text{sky\_vis} = \frac{\sum_{\text{az}=1^\circ}^{360^\circ} \text{ele}_{\text{az}}}{90^\circ \times 360^\circ} \tag{1}$$

where ele_{az} is the elevation angle of a particular azimuth angle az, which ranges from 1° to 360°. In this study, we conduct an experiment to investigate the correlation between sky visibility and the positioning errors of different GNSS positioning solutions, namely the errors of a National Marine Electronics Association (NMEA) solution output from a commercial GNSS receiver, a conventional weighted least squares (WLS) method, a GNSS shadow matching method (Wang et al. 2013), and a skymask-based 3DMA GNSS method (Ng et al. 2020). The results are shown in Fig. 2. The experimental locations are shown in the experimental and result sections.

The settings of these algorithms are as follows,

1. Conventional WLS: This algorithm is based on the open-source code of GoGPS version 0.4.3 (Herrera et al. 2015).
2. Shadow matching: The satellite visibility is labeled by the ground truth location and 3D building model, and the hypothesized grids are distributed based on the ground truth location. The radius of the searching circle is 30 m (Wang et al. 2013).
3. Skymask-based 3DMA GNSS: This is a computationally efficient ray-tracing 3DMA GNSS method and has the same setting as (2) (Ng et al. 2020).

From Fig. 2, it is clear that the performance of these algorithms varies with sky visibility, with each algorithm performing best in different sky visibility conditions. Thus, we aim to develop an algorithm that can estimate the sky visibility and detect the context of urban canyons.

For a context-aware algorithm, the context is the surrounding environment of the user, and the environment is categorized as indoor, outdoor, or semi-outdoor (Zhou et al. 2012). Most context-aware approaches use information from an inertial measurement unit (IMU) (Capurso

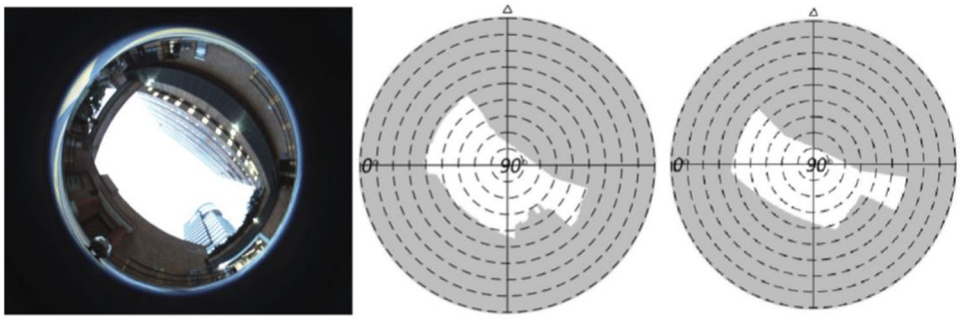

Fig. 1 Demonstration of an image from a fish-eye camera (left), the skymask from the fish-eye image (middle), and the skymask from a 3D building model (right). There are slight sky visibility differences between the two skymasks

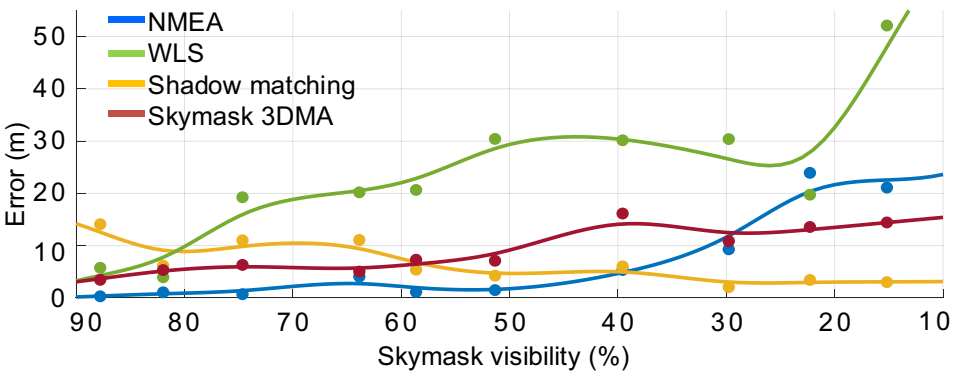

Fig. 2 Performance of different GNSS solutions in different sky visibility conditions

et al. 2017), Wi-Fi, GNSS signals (Groves et al. 2013), Bluetooth signals (Zou et al. 2016), cellular signals (Wang et al. 2016), or a sound probe (Sung et al. 2015). For context detection algorithms using GNSS signals, the received signal strength and the number of received satellites are the input features that are used to train the classifier to categorize the environment as outdoor or indoor (Gao and Groves 2018). Furthermore, the GNSS signals give an indication of the environment category and can also be used to describe the surrounding environments. For example, research reveals that the reflection of GNSS signals can be used to rectify the 2D position of building models (Wada et al. 2017). Other recent work shows that the visibility of a GNSS satellite may be used to classify the environmental situation of around railways (Tan et al. 2019).

Our major innovation is to use the visibility of the satellites, which is obtained using the above-mentioned GNSS features, to categorize the outdoor environment in terms of sky visibility. To the best of our knowledge, this is the first attempt to estimate the sky visibility and the boundary of surrounding buildings (i.e., the skymask) using only the GNSS signal, without using information from 3D building models or fish-eye camera images. Crucially, this means our algorithm could be embedded in most GNSS receivers, even those without connectivity.

An overview of the proposed method is given in the following section. Subsequently, the detail of the proposed sky visibility estimation algorithm is introduced. Then, simulation and experiment results are evaluated. Finally, conclusions are drawn, and future work is suggested.

Overview of the proposed sky visibility estimation algorithm

The flowchart of the proposed skymask estimation algorithm is shown in Fig. 3. The GNSS measurements and ephemeris data of satellites are used as the inputs. To classify the visibility of satellites, features that are related to satellite visibility are extracted. For the RINEX level LOS/NLOS classification (Yozevitch et al. 2016; Hsu 2017; Sun et al. 2019), features include C/N_0, elevation angle, pseudorange residuals, and pseudorange rate. These features can be acquired from the raw measurements, and position can be estimated by directly using conventional WLS. The accuracy of the LOS/NLOS classification can be further improved if the correlator-level measurements are available (Xu and Luo 2019), and if the deep learning approach is applied for detecting the NLOS and the multipath for indoor positioning (Liu et al. 2019).

The classification reveals the visibility of satellites as LOS or NLOS. In addition, the elevation and azimuth angles of the non-tracked satellites are calculated from the approximate user position and the satellite ephemeris data.

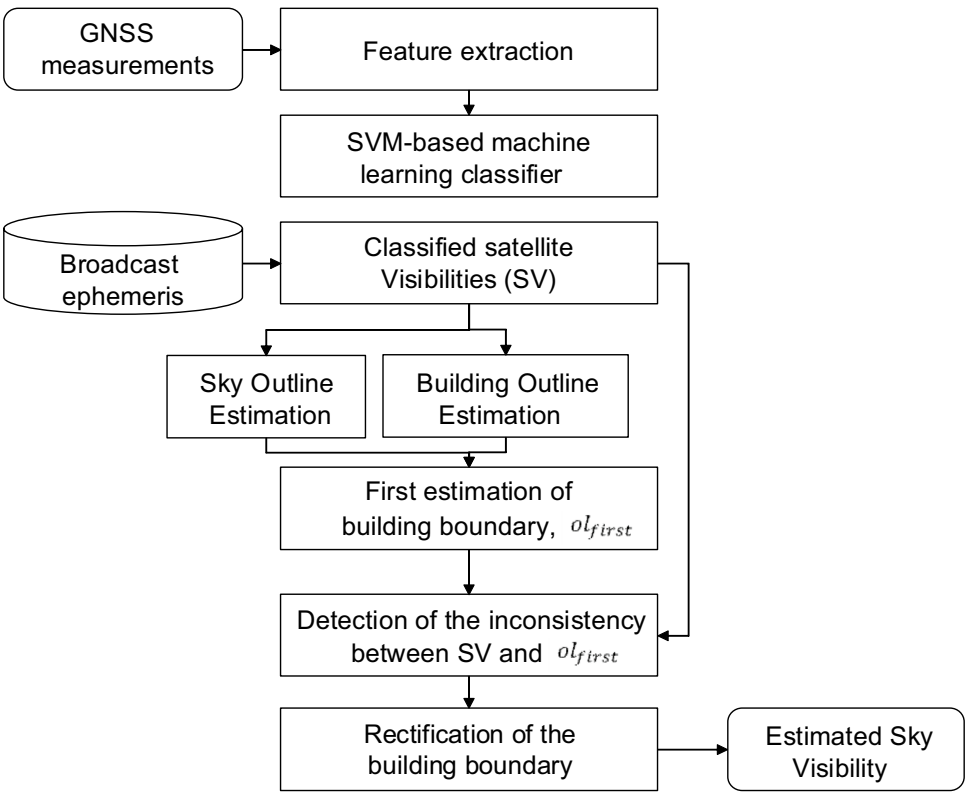

Fig. 3 Flowchart of the proposed skymask estimation algorithm. After several steps, the sky visibility of the user position can be derived from the GNSS measurements (where SVM = support vector machine)

The non-tracked satellite signal is usually considered to be blocked by the surrounding buildings, and this satellite is therefore denoted as NLOS. Thus, by taking the non-tracked satellites into consideration, more information can be garnered on building geometry.

Based on the visibility of satellites, the skymask can be estimated by the following steps. For an LOS satellite, the signal is directly acquired by the receiver, which means that the elevation angle of the satellite is greater than the highest elevation angle of the surrounding building edges over the same satellite azimuth angle. Thus, a large number of LOS satellites can provide elevation angles without blockage over many azimuth angles, which can be used to estimate the sky outline. Analogously, as an NLOS satellite has a lower elevation angle, its signal is blocked by the surrounding buildings, which means that the azimuth and elevation angles of a large number of NLOS satellites can be used to estimate a building outline. The satellite information for skymask estimation is shown in Table 1. The skymask generated from LOS, NLOS, and non-tracked satellites data is shown in Fig. 4.

Moreover, it is obvious that the elevation angles of building boundaries are between those of the sky and building outlines. Thus, if the estimation of the building boundary is accurate, the difference between the real and estimated skymask is small enough to be used to categorize the different levels of an urban canyon.

Sky visibility estimation algorithm

Three kinds of outlines are estimated: sky outline, building outline, and building boundary (Fig. 4). The outline can be described as a subset of elevation angles indexed by azimuth angles and is therefore denoted as

$$\mathrm{ol}(\mathrm{az}) = \mathrm{ele} \quad \text{where az} = 1°, 2°, \ldots, 360°$$

A brief description of the algorithm is given as follows. First, the elevation and azimuth angles of LOS and NLOS can be used to predict the sky and building outlines, respectively, using a curve-fitting function. Then, the building boundary is obtained by combining appropriately weighted sky and building outlines. Then, since the first estimation of the building boundary may be inconsistent with the satellite visibility as LOS or NLOS, we rectify the building boundary based on the inconsistency. The detail of the algorithms is presented in the following subsections.

Table 1 Use of different types of satellites in the proposed skymask estimation

	Visibility	Usage
Satellite type		
Tracked and classified	LOS	Sky estimation
	NLOS	Blockage estimation
Non-tracked	NLOS	Blockage estimation

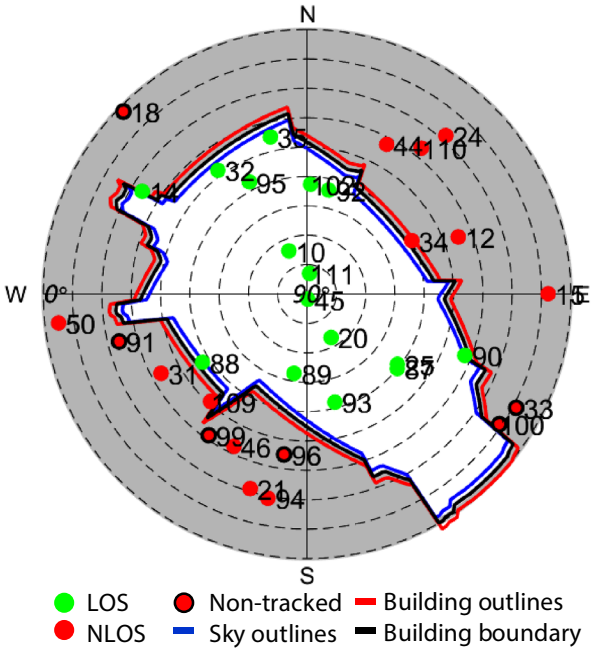

Fig. 4 Demonstration of the skymask obtained from signals from LOS, NLOS, and non-tracked satellites. In this urban area, some satellites cannot be tracked by the receiver

Sky outline estimation algorithm

Here, the elevation and azimuth angles of LOS satellites are used to fit a curve that represents the outline of a clear sky. From Fig. 4, it can be seen that if two LOS satellites are located at a similar azimuth angle, the LOS satellite with a low elevation angle is closer to the sky outline than that with a high elevation angle. Therefore, LOS satellites with a high elevation angle contribute less to the estimation.

Moreover, LOS satellites with relatively low elevations are selected to compute the elevation angle of the skyline in the first estimation of the building boundary. Briefly, we examine a 10° range of the azimuth angle, and if this range contains more than one LOS satellite, we select the LOS satellite with the lowest elevation angle. The selected LOS satellites are then used in a curve-fitting function to generate the sky outline. However, there may be situations where most satellite signals are blocked by the surrounding buildings in deep urban canyons; in such a case, the number of LOS satellites is very low, and thus there are insufficient data for estimating the sky outline across 360° of azimuth angles. An example of this situation is

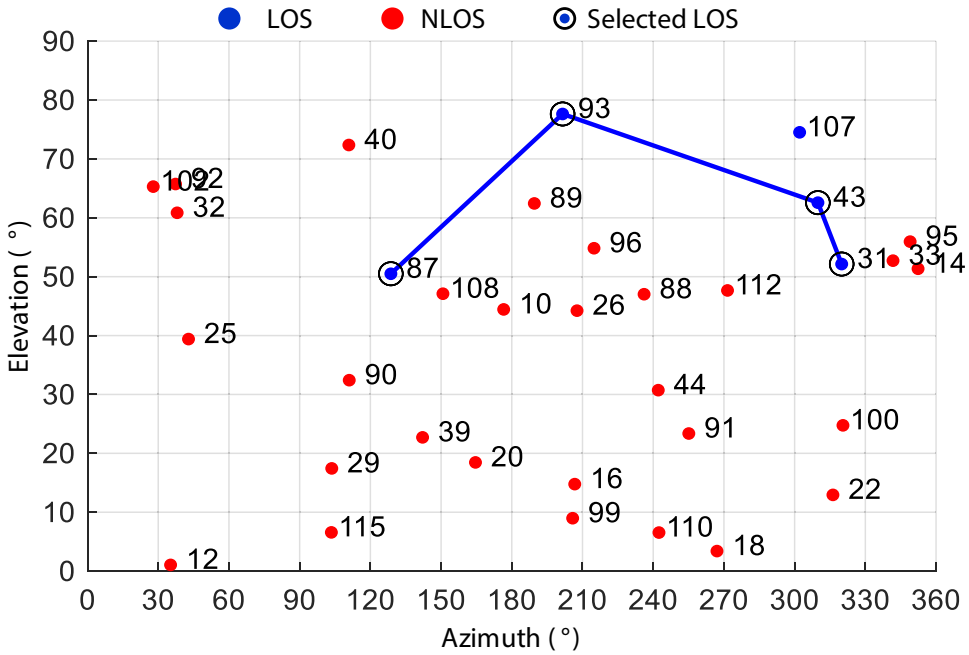

Fig. 5 Example of a spread skyplot of satellite distribution in a deep urban canyon. The number indicates the pseudo-random noise (PRN) of the satellite

shown in Fig. 5, wherein it can be seen that there is no LOS satellite in the azimuth angle range of 0–120°, thus making it difficult to estimate the skyline. Therefore, a threshold for skyline estimation should be set, based on the number of selected LOS satellites, such that when the number of selected LOS satellites is less than this threshold, the skyline is impossible to be estimated and set to a default elevation angle of 90° for every azimuth angle. In our algorithm, the threshold of selected LOS satellites is set as 5.

In addition, two unsatisfactory types of satellite distribution lead to poor satellite geometries and thus poor estimation. First, a poor distribution of satellites will lead to an azimuth gap between two selected satellites that is too large, thus negatively affecting the estimation. Second, if the elevation angle of the selected satellite is far away from the building boundary, a large elevation gap will exist in the

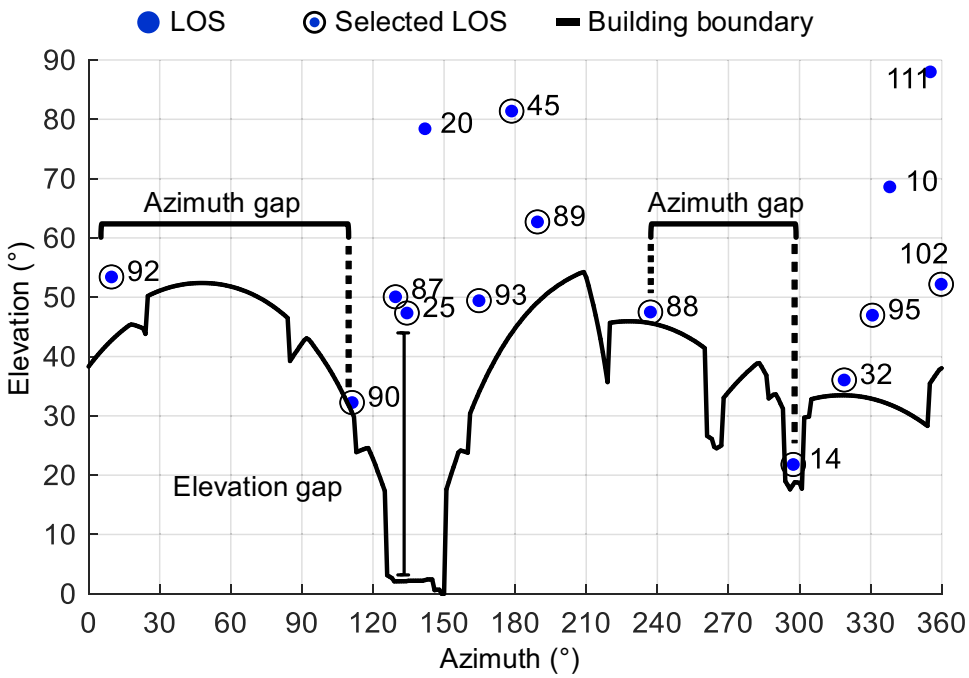

Fig. 6 Demonstration of a substandard spread skyplot showing gaps in azimuth and elevation angles that results from poor satellite geometry. The number indicates the PRN of a satellite

estimation. The results of these poor satellite geometries are demonstrated in Fig. 6.

To mitigate the effect of azimuth gap, we use different approaches according to the category of the azimuth angle gap, as shown in Table 2. The small-sized gap is ignored. Thus, for a middle-sized gap, we hypothesize two virtual satellites by linear interpolation from the two satellites that form the gap. For a large-sized gap, we hypothesize that virtual satellites with a default elevation angle (85° for skyline estimation) are located within these azimuths.

The sky outline, s, is estimated by fitting the LOS satellites into a smoothing spline model, which is an optimization problem. Its cost function is given as follows:

$$\arg\min_{\mathrm{ol}_{\mathrm{sky}}} \left(p \sum_i w_{i.\mathrm{los}} \left(\mathrm{ele}_i - \mathrm{ol}(\mathrm{az}_i)\right)^2 + (1-p) \int_{0°}^{360°} \left(\frac{\mathrm{d}^2 \mathrm{ol}_{\mathrm{sky}}(\mathrm{az})}{\mathrm{daz}^2} \right)^2 \mathrm{daz} \right) \tag{2}$$

where az_i and ele_i denote the azimuth and elevation angles of the LOS satellite i, respectively, p denotes a smoothing parameter that is tuned heuristically, and w_i is the weighting given the satellite i. The weighting is calculated as follows:

$$w_{i.\mathrm{los}} = k \cdot \sqrt{1 - \frac{\mathrm{ele}_i}{90}} \tag{3}$$

where k is a scaling factor that is heuristically set to 100. The lower the elevation the weighting scheme is based on, the higher the weighting. By this optimization procedure, the sky outline can be effectively estimated even in conditions of poor satellite geometry. A result of the proposed skyline estimation is demonstrated in Fig. 7, and the algorithm is summarized in Fig. 8.

Table 2 Categories of azimuth angle gap and how these are mitigated

	Category	Approach
Azimuth gap (°)		
0–60	Small	Ignore
60–120	Middle	Hypothesize virtual satellites and set their elevation angles by linear interpolation
120–360	Large	Hypothesize virtual satellites and assign these a default elevation angle

Building outline estimation algorithm

The building outline estimation procedure is similar to that of the sky outline estimation but uses NLOS satellites. After selecting the blocked satellites, this procedure also encounters similar problems to those seen in the sky outline estimation, namely low satellite numbers, resulting in azimuth and elevation gaps. As before, certain categories of satellites

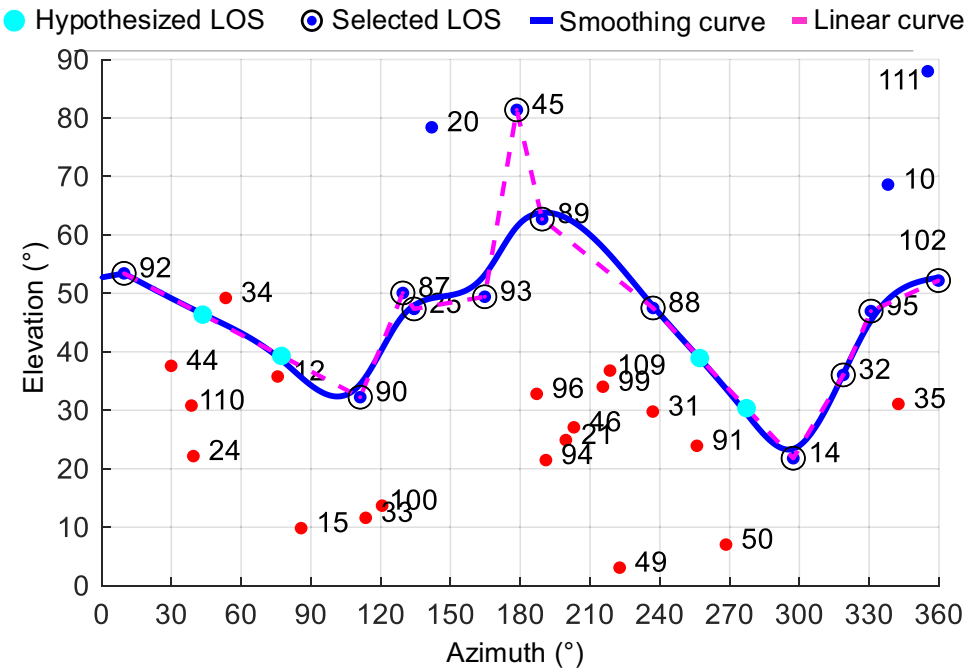

Fig. 7 Example of the proposed sky outline estimation algorithm. The weighting scheme and hypothesized satellites mitigate the effects of gaps on azimuth and elevation

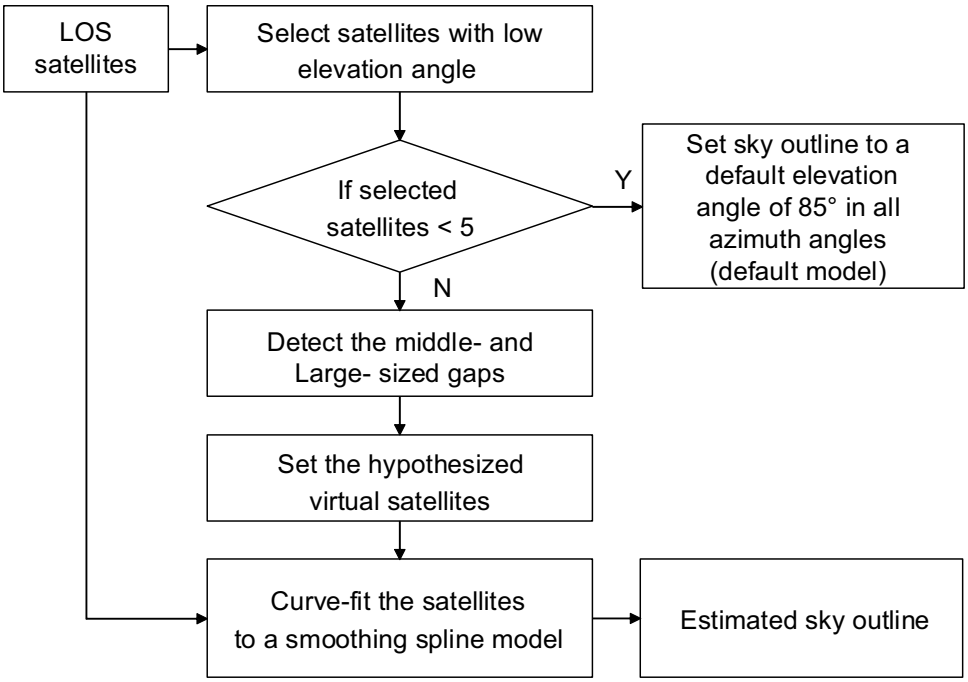

Fig. 8 Flowchart of the sky outline estimation

are hypothesized to fill the azimuth gap, and the weight of a blocked satellite i is calculated as

$$w_{i.\mathrm{nlos}} = k \cdot \sqrt{\frac{\mathrm{ele}_i}{90}} \tag{4}$$

The weighting scheme is designed such that the higher the elevation of the NLOS satellite, the higher its weight. The default elevation of a hypothesized satellite in a large azimuth gap is 5°. An example is shown in Fig. 9.

Building boundary estimation algorithm

Once the outlines of the sky and the buildings are obtained, the building boundary can be estimated by a weighting method. The estimated elevation of the boundary is expressed as

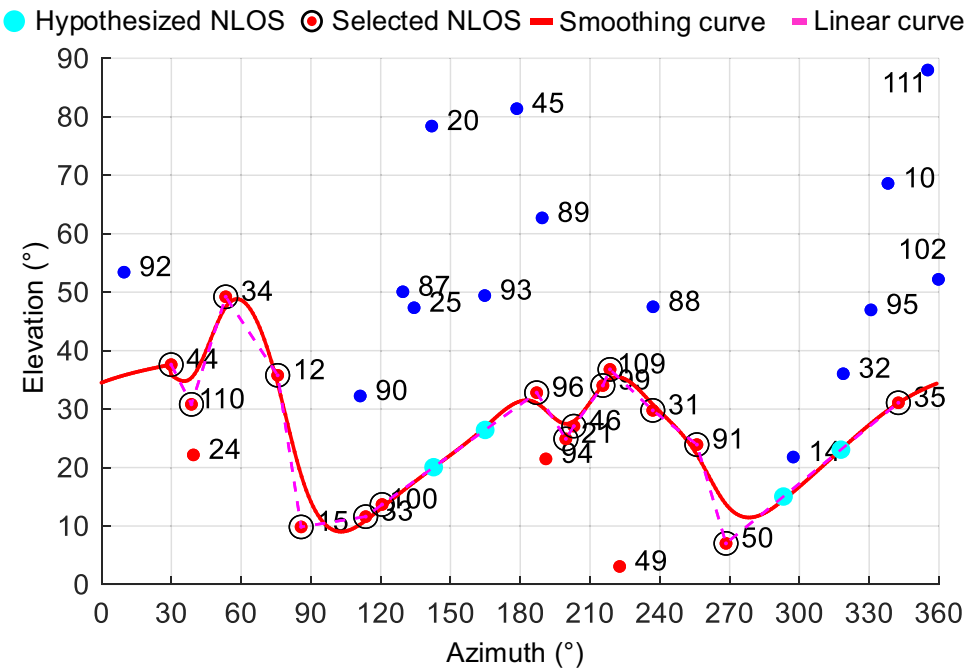

Fig. 9 Example result of the proposed building outline estimation algorithm. The weighting scheme and hypothesized satellites are also applied in this case

$$\mathrm{ele}^{i}_{\mathrm{boundary}} = \mathrm{ele}^{i}_{\mathrm{sky}} * w_{\mathrm{scene}} + \mathrm{ele}^{i}_{\mathrm{building}} * w^{-1}_{\mathrm{scene}} \tag{5}$$

where $\mathrm{ele}^{i}_{\mathrm{sky}}$ and $\mathrm{ele}^{i}_{\mathrm{building}}$ are the estimated elevation at azimuth i of the skyline and the building, respectively, and w_{scene} is a weighting factor. The weighting method is designed to make adaptive changes under different levels of sky visibility. For example, in an area with high sky visibility (i.e., a relatively open sky area), the weight of the building outline is greater than that of the sky outline, since there is sufficient sky outline information, and we wish to abstract more building information. Conversely, in a deep urban canyon, there is abundant building outline information but insufficient sky outline information, and thus a higher weighting is given to the sky outline in this case. Accordingly, we use a scene-adaptive weighting scheme that is calculated by

$$w_{\mathrm{scene}} = \frac{N_{\mathrm{nlos}} + N_{\mathrm{non\_tracked}}}{N_{\mathrm{los}}} \tag{6}$$

where N_{los}, N_{nlos}, and $N_{\mathrm{non\_tracked}}$ are the number of LOS satellites, NLOS satellites, and non-tracked satellites, respectively. The estimated building boundary (skymask) of low (left), middle (middle), and high (right) sky visibility with boundary estimation is shown in Fig. 10.

From Fig. 10, it can be seen that the estimated boundary indicates the extent of sky visibility and is close to the real building boundary. However, the estimated boundary disagrees with the classified visibility of the satellite (i.e., LOS and NLOS) in some azimuths, as shown in the deep urban case. The inconsistent satellites are highlighted in the figure, and these satellites are grouped into a subset that is denoted as $\mathrm{SV}_{\mathrm{inconsistent}}$. These inconsistencies are caused by the fitting method and the fact that the weighting function is not perfect; as a result, the first estimated boundary must be rectified to match the actual satellite visibility.

Boundary rectification algorithm

To solve the inconsistency of the satellite visibility, we adjust the elevation angle of the first estimated boundary as follows:

$$\mathrm{ol}_{\mathrm{adjusted}}(\mathrm{az}_j) = \begin{cases} \mathrm{ol}_{\mathrm{first}}(\mathrm{az}_j) - \mathrm{ele}_{\mathrm{bias}}, & \text{if sv } j \text{ is LOS} \\ \mathrm{ol}_{\mathrm{first}}(\mathrm{az}_j) + \mathrm{ele}_{\mathrm{bias}}, & \text{if sv } j \text{ is NLOS} \end{cases} \quad \text{where } j \in \mathrm{SV}_{\mathrm{inconsistent}} \tag{7}$$

where $\mathrm{ele}_{\mathrm{bias}}$ is the elevation bias used to include the building-edge uncertainty and is set as 3°. After this, the adjusted building boundary is again optimized by (2) to fit the smooth spline model and thus to rectify the building boundary. The weighting factor should be revised to account for the azimuth angle of the inconsistency (az_j, $j \in \mathrm{SV}_{\mathrm{inconsistent}}$). We empirically set the weighting of these adjusted elevation angles to be three times more than that of the non-adjusted elevation angles. The resulting rectified building boundary, which we denote a skymask, is shown in Fig. 11. The rectified boundary estimation is closer to the actual building outline, as compared to the first boundary estimation.

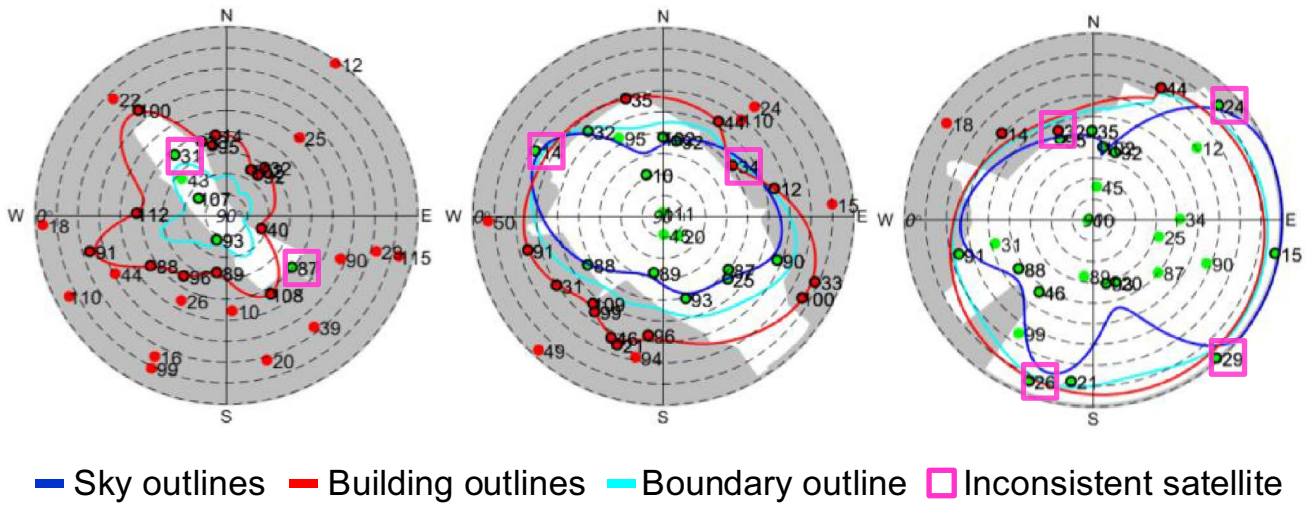

Fig. 10 Example of the first estimation of building boundaries in different sky visibility situations. The first estimation provides approximate sky visibility, with some satellites being inconsistent with the estimated visibility boundary

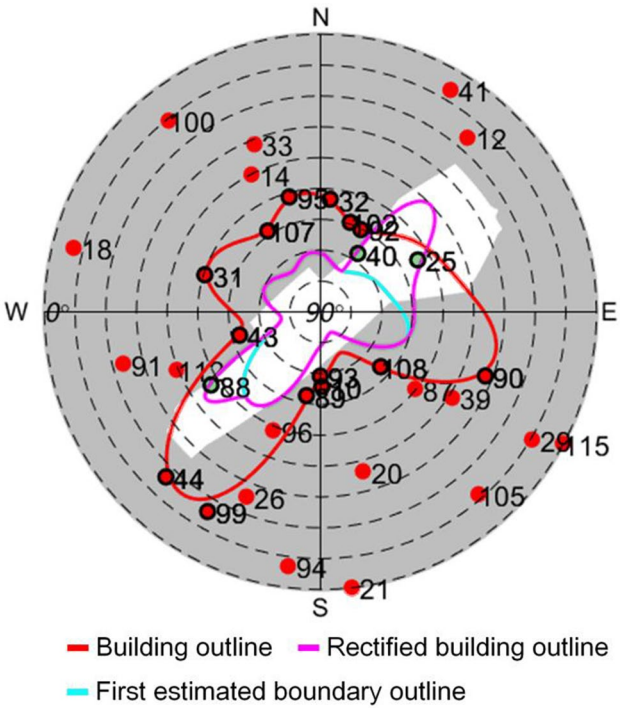

Fig. 11 Demonstration of the building boundary estimation before (first estimation) and after rectification. The rectification improves the performance of sky visibility estimation

After considering the inconsistency of the satellite visibility, the sky visibility can be estimated based on the rectified building boundary:

$$\text{sky\_vis} = \frac{\sum_{\text{az}=1^\circ}^{360^\circ} \text{ol}_{\text{rectified}}(\text{az})}{90^\circ \times 360^\circ} \tag{8}$$

The estimated sky visibility indicates the percentage of the sky from the user location, which could be considered as a reference for different positioning approaches as mentioned in the Introduction section.

To summarize, the proposed method first uses the raw GNSS measurements to classify the GNSS signal visibilities as LOS or NLOS, and then these visibilities are used to determine the sky visibility of the environment in which the receiver is located. The performance of the proposed method is evaluated in the following section.

Experiment and results

To verify the proposed skymask estimation algorithm, we performed static experiments at 10 different locations in Hong Kong, as shown in Fig. 12 (top). At each location, a u-blox F9T receiver was used to collect approximately 15 min of GNSS signals, namely GPS, GLONASS, and

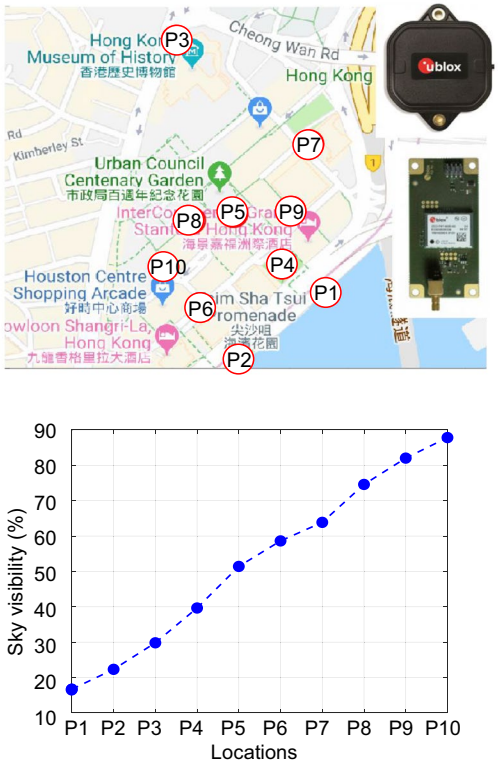

Fig. 12 Locations of the static experiments in urban canyons of Hong Kong (from Google Maps) (top), and the sky visibilities of these locations (bottom)

BeiDou signals. This enabled locations to be sorted by sky visibility, from low to high, as shown in the bottom panel.

We first evaluate the proposed method based on the perfect LOS/NLOS classifications of the data, which are made by reference to ground truth location and a 3D building model. We also evaluate the proposed method by altering the LOS/NLOS classification accuracy. Finally, we discuss the result of the proposed skymask estimation, based on our previously developed machine learning classifier (Hsu 2017).

Performance with the perfect LOS/NLOS classification

In this experiment, the LOS/NLOS classification is based on the ground truth location and the surrounding 3D building models, where the latter are obtained from Google Earth and have an accuracy of approximately 1 m. In Table 3, the mean and standard deviation of the sky visibility of the estimated boundary are compared with the real-sky visibility.

According to Table 3, the difference between the estimated and the real-sky visibilities is less than approximately 5% in most of the locations, and the estimated sky visibility is stable, with a standard deviation of less than 3%. However, the estimation of sky visibility in a deep urban area, such as

Table 3 Mean and standard deviation of the real and estimated sky visibility at different locations in Hong Kong

Locations	P1	P2	P3	P4	P5	P6	P7	P8	P9	P10
Real-sky visibility (%)	16.69	23.20	29.82	39.66	51.42	58.63	63.88	74.61	82.04	87.85
Mean of estimated visibility (%)	25.74	27.31	25.97	44.60	46.12	61.69	60.47	68.78	82.78	86.16
SD of estimated visibility (%)	0.96	2.74	1.90	0.58	0.58	1.13	2.43	1.24	1.32	2.18

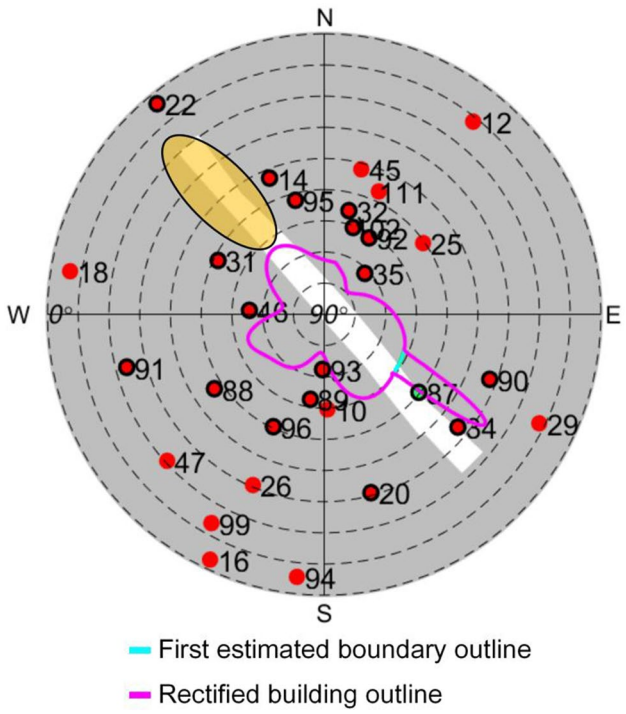

Fig. 13 Demonstration of the estimated building boundary in a deep urban canyon (P1) before and after the rectification. The brown-shaped ellipse indicates an estimated area that is not able to be rectified, due to the poor geometry of satellites providing insufficient information. The rest of the first estimated boundary in the diagram has the same geometry as the rectification

P1, is poor. This is primarily attributable to the limited number of LOS satellites visible from these deep urban areas. The skymask of P1 with boundary estimation and rectification is shown in Fig. 13.

In the P1 case, there is only one LOS satellite visible, which makes it difficult to find the correct sky outline. For example, the estimation of the framed area cannot be rectified by data from LOS satellites, due to the poor satellite geometry. Similar problems exist in the middle urban canyon, P4; its results from two epochs are shown in Fig. 14.

In a short period, no overlap of satellite areas occurs, and thus reference elevations for use in estimation are not available. This underscores that the solution of satellite geometry is a considerable challenge for future improvements to skymask estimations in these urban canyon environments.

Performance with different LOS/NLOS classification accuracies

Classification accuracy is vital to the performance of the proposed algorithm because the estimations of the sky and building outlines are largely based on satellite visibility. To delineate the effect of classification accuracy on sky visibility estimation, we simulate the performance of the proposed estimation algorithm utilizing data with different classification accuracies, where the minimum accuracy is 50%. When the classification accuracy is less than 50% accurate, the

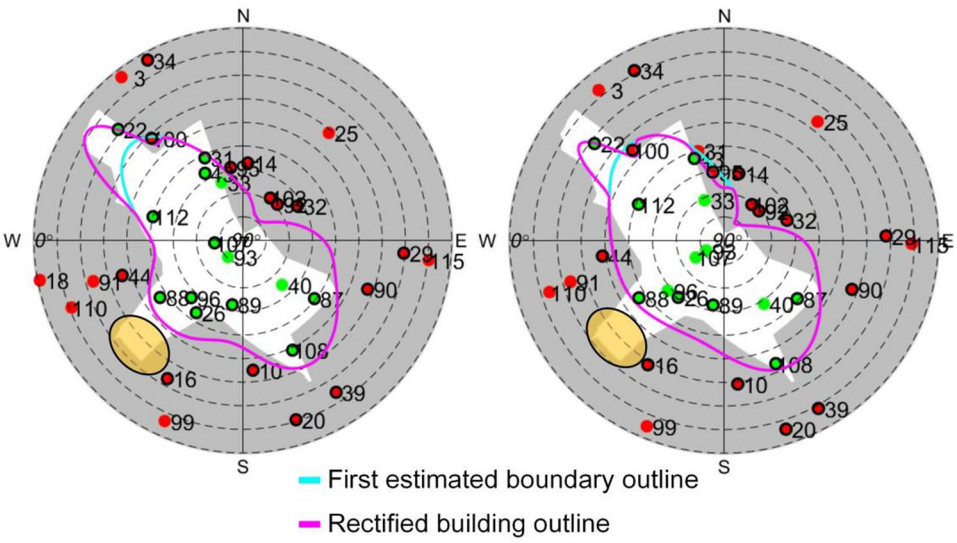

Fig. 14 Skymask of P4 with boundary estimation and rectification at epoch 1 (left) and epoch 724 (right). The brown-shaped ellipse indicates estimated areas that cannot be rectified due to poor satellite geometry providing insufficient information

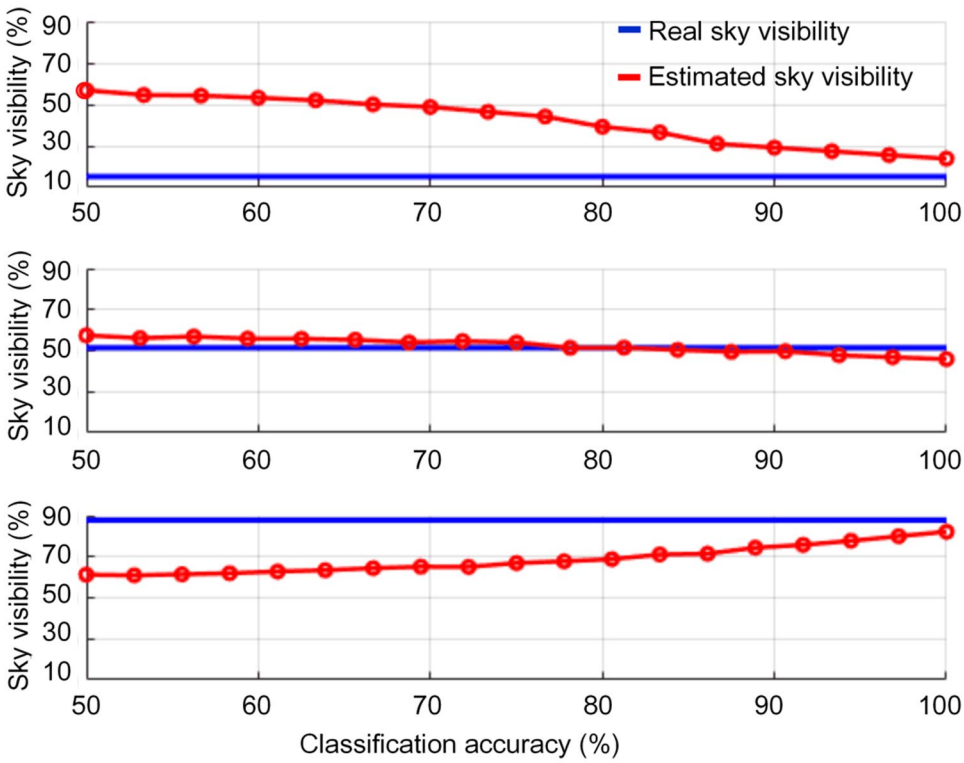

Fig. 15 Mean of estimated sky visibility with different classification accuracies in low real-sky visibility (top), medium real-sky visibility (middle), and high real-sky visibility (bottom) situations

classification method is less accurate than tossing a coin. For the classification simulation, the satellite visibility is classified by ground truth and 3D building models, and then a random satellite is selected and its visibility is switched to the other type. In this manner, the classification accuracy is decreased as the number of satellites selected increases. We run this simulation 100 times, and the mean of the sky visibility estimated by the proposed algorithm with different classification accuracies utilized is shown in Fig. 15.

From Fig. 15, it can be seen that the performance of the algorithm in low and high real-sky visibility situations is highly correlated with the classification accuracy. In these situations, there are few satellites of one kind of satellite visibility, i.e., few LOS satellites in the low real-sky visibility (deep urban) situation, or few NLOS satellites in the high real-sky visibility (slight urban) situation. Therefore, the outlines estimated from these situations will be far from the real outlines when these satellites are misclassified.

However, it is interesting to note that in the medium real-sky visibility situation (Fig. 15, middle), the estimated sky visibility is insensitive to the classification accuracy. This is attributable to the failure of the LOS/NLOS classification, which results in the mean elevation angle of estimated boundary outlines being nearly 45° according to the weighting method of the proposed algorithm, which thus makes the sky visibility approximately 50%. The skymask for middle real-sky visibility (middle urban) with boundary estimation and rectification, which shows a 50% and 100% classification accuracy, is shown in Fig. 16. As can be seen, different classification accuracies have only a minimal effect on the estimated sky visibility in medium-urban areas.

Performance with two different LOS/NLOS classification approaches

In this section, two kinds of conventional classification algorithms are used: a simple signal-to-noise ratio (SNR) classifier and an SVM-based machine learning classifier incorporating several GNSS features (Hsu 2017). The SNR is typically used to indicate the quality of the received signal. In general, an NLOS satellite gives a low received signal strength; thus, a simple threshold of SNR can be set to classify satellite visibility. For our u-blox F9T device, we set the SNR threshold to 35 dB and define the satellite visibility as

$$\text{Visibility} = \begin{cases} \text{LOS} & \text{if SNR} \geq 35\,\text{dB} \\ \text{NLOS} & \text{if SNR} < 35\,\text{dB} \end{cases}. \tag{9}$$

The accuracy of SNR classification and the mean of estimated sky visibility are shown in Tables 4 and 5, respectively.

As shown in Table 4, the classification accuracy of P1 is 92.1% and its mean estimated sky visibility is 27.51%, which is similar to the performance obtained with perfect classification (25.74%). In addition, the estimated sky visibilities of P8, P9, and P10 are close to 60%, which matches

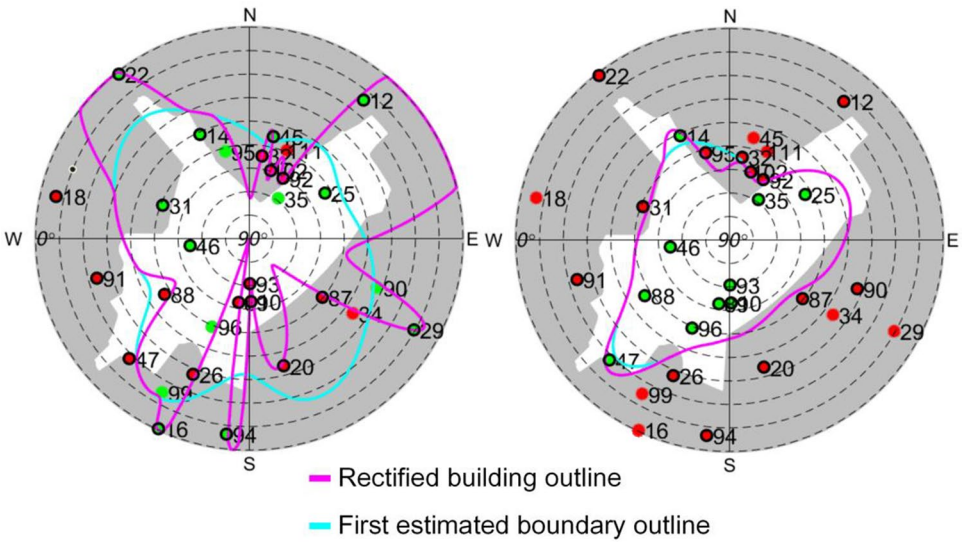

Fig. 16 Demonstration of the skymask in medium-urban areas, with boundary estimation and rectification, and using data with 50% classification accuracy (left) and 100% classification accuracy (right)

Table 4 Classification accuracy of SNR classification

Location	P1	P2	P3	P4	P5	P6	P7	P8	P9	P10
Classification accuracy (%)	92.1	85.5	86.2	78.5	83.8	80.0	77.3	62.5	65.3	68.4

Table 5 Mean and standard deviation of sky visibility according to SNR classification

Location	P1	P2	P3	P4	P5	P6	P7	P8	P9	P10
Real visibility (%)	16.69	23.20	29.82	39.66	51.42	58.63	63.88	74.61	82.04	87.85
Mean of estimated visibility (%)	27.51	32.92	29.34	37.00	48.76	51.72	47.66	52.40	57.82	60.60
STD of estimated visibility (%)	2.37	5.59	4.06	6.18	2.77	5.56	3.67	5.16	0.90	2.37

the earlier simulations of classification accuracy in slight urban locations. For the medium-urban canyons P4 and P5, the mean of the estimated sky visibility is close to the real visibility, since there are enough satellites to aid both sky outline and building outline estimation.

It can be seen from Table 5 that the standard deviation of the estimated sky visibility according to SNR classification varies greatly. In comparison with that of perfect classification, the standard deviation of the estimated sky visibility with SNR classification is greater than 3% in most of the locations. This is because the SNR classification of satellite visibility changes greatly across a range of epochs, thus causing substantial variations in building boundary estimation. The skymasks at P6, with boundary estimation and rectification by SNR classification at epochs 130, 131, and 132, are shown in Fig. 17.

From Fig. 17, it can be seen that satellites 25, 87, 89, and 93 are misclassified as NLOS at epoch 130 (top) and that satellite 25 is correctly classified as LOS at epoch 131 (middle). This leads to a larger sky outline and higher sky visibility at epoch 131 compared with that at epoch 130. Moreover, by comparing the visibility at epoch 131 with that at epoch 132, the NLOS satellite 34 is misclassified as LOS at epoch 132 (bottom), accounting for an approximately 5% increase in the estimated sky visibility. Overall, the misclassification and inconsistency of SNR classification result in a relatively large error with a large standard deviation.

In the proposed algorithm, an SVM classification is used, comprising the following features: signal-to-noise ratio (SNR), elevation angle, normalized pseudorange residual, and pseudorange rate consistency (Hsu 2017). The kernel function of SVM classification is a radial basis function, and the SVM model is trained by the dataset of 60 percent of samples, which are randomly selected from all locations. The SVM classification accuracy is shown in Table 6, and the mean and standard deviation of the estimated sky visibility based on the SVM classification are shown in Table 7.

It can be seen in Table 6 that the SVM classification accuracy of P1, P2, and P3 exceeds 95%, showing that the estimation of these locations is close to that obtained from perfect classification. In addition, the differences in the mean of the estimated sky visibility between SVM classification and perfect classification are only 0.94%, 0.72%, and 1.29%

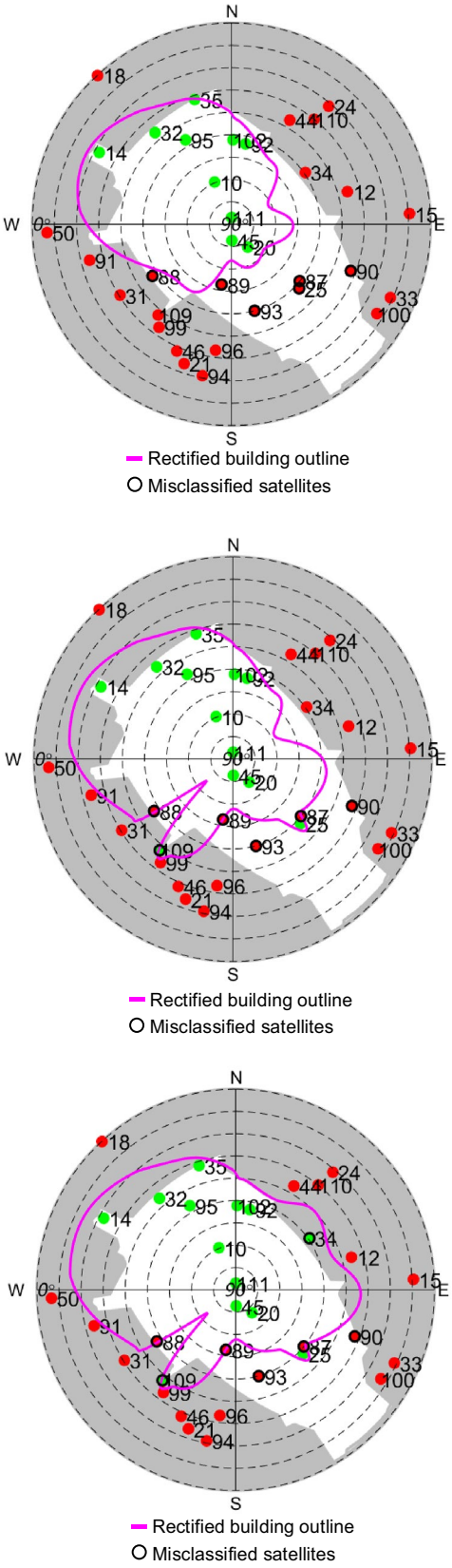

Fig. 17 Demonstration of the skymask with boundary estimation and rectification at P6 in three epochs. At epoch 130 (top), the estimated sky visibility is 42.91%. At epoch 131 (middle), the estimated sky visibility is 51.48%. At epoch 132 (bottom), the estimated sky visibility is 56.25%

for P1, P2, and P3, respectively. However, due to the imperfect satellite distribution, biases remain in these sky visibility estimations.

Conclusions and future work

We develop a sky visibility estimation algorithm based on satellite visibility. We estimate the outlines of sky and buildings by fitting the curve of data into a smoothing spline model, and the boundary of surrounding buildings is then computed by an adaptive weighting scheme that reveals the scene at the receiver's location. Moreover, the boundary estimation is rectified to eliminate the inconsistencies between the classified satellite visibility and the first estimated building boundary. If a perfect LOS/NLOS classification is available, the proposed sky visibility estimation can achieve a result very similar to the actual sky visibility. Furthermore, even if only a machine learning-based classifier is available, the proposed method can still obtain good performance in middle and deep urban canyons, where such performance is needed most.

Sky visibility can identify different levels of urban coverage and is known to affect the performance of different positioning systems. In future work, we will use our method to improve the performance of a loosely coupled GNSS/INS (integrated navigation system). In addition, we will improve our classification with different types of signals, and its ability to deal with the many reflected and refracted signals from various obstructions in urban areas, such as trees or power lines. The effect of these obstructions on signal features, e.g., frequency, correlation value, and chip delay, needs to be further researched with the use of a software-defined receiver.

Currently, our estimation algorithm uses the epoch-by-epoch visibility of satellites without considering their temporal connectivity, and the least-squares positioning is only used for deriving features for signal classification. Thus, we will also attempt to take a raw position as environmental information to improve the performance of our algorithm since this raw information may vary according to its environments, such as deep urban, middle urban, slight urban, and open sky. Moreover, with an exact building boundary estimation, this algorithm will be applied to the selection of different positioning approaches, which will contribute to the development of a context-aware navigation scheme (Groves et al. 2013).

Table 6 Accuracy of SVM classification

Location	P1	P2	P3	P4	P5	P6	P7	P8	P9	P10
Classification accuracy (%)	96.2	95.3	95.6	89.6	91.7	85.5	86.4	80.7	67.0	72.5

Table 7 Mean and standard deviation of sky visibility by SVM classification

Location	P1	P2	P3	P4	P5	P6	P7	P8	P9	P10
Real visibility (%)	16.69	23.20	29.82	39.66	51.42	58.63	63.88	74.61	82.04	87.85
Mean of estimated visibility (%)	26.68	26.59	24.68	37.19	44.03	50.01	48.09	64.53	58.80	62.36
STD of estimated visibility (%)	0.96	3.52	1.88	3.38	1.89	2.96	3.09	2.48	1.80	2.05

Acknowledgements The authors acknowledge the support of the Hong Kong PolyU startup fund on the project 1-ZVKZ, "Navigation for Autonomous Driving Vehicle using Sensor Integration."

Data availability The associated data are available on request or it can be found in the following link: https://www.polyu-ipn-lab.com/associated-data-in-publication. In the case of the link failed, please contact the corresponding author.

References

Adjrad M, Groves PD (2018) Intelligent urban positioning: integration of shadow matching with 3D-mapping-aided GNSS ranging. J Navig 71(1):1–20. https://doi.org/10.1017/S0373463317000509

Adjrad M, Groves PD, Quick JC, Ellul C (2018) Performance assessment of 3D-mapping-aided GNSS part 2: environment and mapping. J Navig 66(2):363–383. https://doi.org/10.1002/navi.289

Capurso N, Song T, Cheng W, Yu J, Cheng X (2017) An android-based mechanism for energy efficient localization depending on indoor/outdoor context. IEEE Internet Things J 4(2):299–307. https://doi.org/10.1109/JIOT.2016.2553100

Gao H, Groves PD (2018) Environmental context detection for adaptive navigation using GNSS measurements from a smartphone. Navigation 65(1):99–116. https://doi.org/10.1002/navi.221

Groves PD (2011) Shadow matching: a new GNSS positioning technique for urban canyons. J Navig 64(3):417–430

Groves PD, Adjrad M (2017) Likelihood-based GNSS positioning using LOS/NLOS predictions from 3D mapping and pseudoranges. GPS Solut 21(4):1805–1816. https://doi.org/10.1007/s10291-017-0654-1

Groves PD, Martin H, Voutsis K, Walter D, Wang L (2013) Context detection, categorization and connectivity for advanced adaptive integrated navigation. In: Proceedings ION GNSS 2013, Institute of Navigation, Nashville, USA, Sept 16–20, pp 1039–1056

Herrera AM, Suhandri HF, Realini E, Reguzzoni M, de Lacy MC (2015) goGPS: open-source MATLAB software. GPS Solut 20(3):595–603. https://doi.org/10.1007/s10291-015-0469-x

Hsu LT (2017) GNSS multipath detection using a machine learning approach. In: Proceedings of IEEE 20th international conference on intelligent transportation systems (ITSC), Oct 16–19, pp 1–6. https://doi.org/10.1109/itsc.2017.8317700

Hsu LT (2018) Analysis and modeling GPS NLOS effect in highly urbanized area. GPS Solut 22(1):7. https://doi.org/10.1007/s10291-017-0667-9

Hsu LT, Gu Y, Kamijo S (2016) 3D building model-based pedestrian positioning method using GPS/GLONASS/QZSS and its reliability calculation. GPS Solut 20(3):413–428. https://doi.org/10.1007/s10291-015-0451-7

Liu Q, Huang Z, Wang J (2019) Indoor non-line-of-sight and multipath detection using deep learning approach. GPS Solut 23(3):75. https://doi.org/10.1007/s10291-019-0869-4

Ng H-F, Zhang G, Hsu L-T (2020) A computation effective range-based 3D mapping aided GNSS with NLOS correction method. J Navig (**accepted**)

Nicolás ML, Kürner T, Smyrnaios M, Schön S (2013) Ray tracing multipath modelling in GNSS with a single reflector. In: 7th European conference on antennas and propagation (EuCAP), Gothenburg, 2013, pp 2261–2265

Sun R, Hsu L-T, Xue D, Zhang G, Ochieng WY (2019) GPS signal reception classification using adaptive neuro-fuzzy inference system. J Navig 72(3):685–701. https://doi.org/10.1017/S0373463318000899

Sung R, Jung S-H, Han D (2015) Sound based indoor and outdoor environment detection for seamless positioning handover. ICT Express 1(3):106–109. https://doi.org/10.1016/j.icte.2016.02.001

Suzuki T, Kubo N (2012) GNSS positioning with multipath simulation using 3D surface model in urban canyon. In: Proceedings ION GNSS 2012, Institute of Navigation, Nashville, Tennessee, USA, Sept 17–21, pp 438–447

Tan J, Wang J, Lu D (2019) GNSS data driven clustering method for railway environment scenarios classification. In: Proceedings of 14th IEEE conference on industrial electronics and applications (ICIEA), pp 2026–2031. https://doi.org/10.1109/iciea.2019.8833839

Wada Y, Hsu L-T, Gu Y, Kamijo S (2017) Optimization of 3D building models by GPS measurements. GPS Solut 21(1):65–78. https://doi.org/10.1007/s10291-015-0504-y

Wang L, Groves PD, Ziebart MK (2013) GNSS shadow matching: improving urban positioning accuracy using a 3D city model with optimized visibility scoring scheme. Navigation 60(3):195–207. https://doi.org/10.1002/navi.38

Wang W, Chang Q, Li Q, Shi Z, Chen W (2016) Indoor-outdoor detection using a smart phone sensor. Sensors (Basel). https://doi.org/10.3390/s16101563

Xu J, Luo H (2019) Intelligent GPS L1 LOS/multipath/NLOS classifiers based on correlator-, RINEX- and NMEA-level measurements. Remote Sens. https://doi.org/10.3390/rs11161851

Yozevitch R, Moshe BB, Weissman A (2016) A robust GNSS LOS/NLOS signal classifier. Navigation 63(4):429–442. https://doi.org/10.1002/navi.166

Zhou Pengfei, Zheng Yuanqing, Li Zhenjiang, Shen Guobin (2012) IODetector: a generic service for indoor/outdoor detection. ACM Trans Sensor Netw 11:361–362. https://doi.org/10.1145/2426656.2426709

Zou H, Jiang H, Luo Y, Zhu J, Lu X, Xie L (2016) BlueDetect: an ibeacon-enabled scheme for accurate and energy-efficient indoor-outdoor detection and seamless location-based service. Sensors (Basel) 16(2):268. https://doi.org/10.3390/s16020268

Haosheng Xu received a B.Sc. in Thermal Energy and Power Engineering from Jilin University, China, in 2016 and an M.Sc. at the Department of Mechanical Engineering, The Hong Kong Polytechnic University (PolyU), Hong Kong, in 2019. He is currently a research assistant at the Interdisciplinary Division of Aeronautical and Aviation Engineering, PolyU. His research interests include context awareness-based GNSS navigation and 3D mapping-aided GNSS.

Li-Ta Hsu received the B.S. and Ph.D. degrees in aeronautics and astronautics from National Cheng Kung University, Taiwan, in 2007 and 2013, respectively. He is currently an assistant professor with the Division of Aeronautical and Aviation Engineering, Hong Kong Polytechnic University, before he served as a post-doctoral researcher in the Institute of Industrial Science at the University of Tokyo, Japan. In 2012, he was a visiting scholar in University College London, UK. He is an Associate Fellow of RIN. His research interests include GNSS positioning in challenging environments and localization for pedestrian, autonomous driving vehicle, and unmanned aerial vehicle.

Debiao Lu received a B.Sc. degree in telecommunication engineering and an M.Sc. degree in traffic information engineering and control from Beijing Jiaotong University, in 2008 and 2010, respectively, where he is currently an Associate Professor with the School of Electronic and Information Engineering. He got his doctor's title with the Faculty of Mechanical Engineering, Technische Universität Braunschweig, under the guidance of Prof. Dr.-Ing. Dr. H.C. Eckehard Schnieder, from 2010 to 2014. His research interests include GNSS performance evaluation for railway applications and safety assurance of GNSS.

Baigen Cai received the B.Sc., M.Sc., and Ph.D. degrees in traffic information engineering and control from Beijing Jiaotong University in 1987, 1990, and 2010, respectively. Since 1990, he has been a faculty member at the School of Electronic and Information Engineering, Beijing Jiaotong University. He was a visiting scholar at the Ohio State University from 1998 to 1999. Currently, he is a professor and the Dean of the School of Computer and Information Technology, Beijing Jiaotong University. His research interests include intelligent transportation systems, GNSS navigation, multi-sensor data fusion, intelligent traffic control, and system modeling and simulation. Prof. Cai is responsible for several national and international cooperation research and development research projects. He is a senior member of IEEE, a member of the Institute of Railway Signal Engineers (IRSE), and serves as a reviewer of many international journals. He is also a member of the Chinese Association of Automation and the Deputy Secretary General of the Committee of Experts on the Chinese Urban Rail Transit Association.